

Ground State of BaFe₂S₃ from Lattice and Spin Dynamics

Y. Oubaid,^{1,2,*} S. Deng,^{3,*} NS. Dhami,¹ M. Verseils,² P. Fertey,² P. Steffens,³ D. Bounoua,⁴
A. Forget,⁵ D. Colson,⁵ P. Foury-Leylekian,¹ M.B. Lepetit,^{6,3,†} and V. Balédent^{1,7,‡}

¹Université Paris-Saclay, CNRS, Laboratoire de Physique des Solides, 91405, Orsay, France.

²Synchrotron SOLEIL, L'Orme des Merisiers, Saint Aubin BP 48, 91192, Gif-sur-Yvette, France

³Institut Laue-Langevin, 71 avenue des Martyrs, 38042 Grenoble, France

⁴Université Paris-Saclay, CNRS-CEA, Laboratoire Léon Brillouin, 91191, Gif sur Yvette, France

⁵Université Paris-Saclay, CEA, CNRS, SPEC, 91191, Gif-sur-Yvette, France.

⁶Institut Néel, CNRS, 38042 Grenoble, France

⁷Institut universitaire de France (IUF)

(Dated: February 20, 2026)

We investigate the interplay between lattice symmetry, phonons, and magnetism in the quasi-one-dimensional ladder compound BaFe₂S₃ by combining polarized synchrotron infrared spectroscopy, hybrid-functional density functional theory calculations, and inelastic neutron scattering. Lattice-dynamics analysis reveals that the crystal symmetry is lower than previously proposed and is consistent with a *P1* space group at low temperature. Several infrared-active phonon modes exhibit pronounced anomalies at both the structural transition temperature $T_S \approx 125$ –130 K and the Néel temperature $T_N \approx 95$ K. First-principles calculations show that the modes affected at T_S predominantly involve displacements that modulate magnetic exchange pathways. Neutron scattering demonstrates that below T_N the magnetic order is three-dimensional, long-ranged, and static. Between T_N and T_S , the system displays three-dimensional short-range dynamic magnetic correlations, which disappear above T_S . The structural transition thus coincides with the onset of magnetic fluctuations rather than with static magnetic order. Our results indicate that short-range, dynamical magnetic correlations are sufficient to drive a static structural instability, providing a magnetically driven mechanism reminiscent of the iron-pnictide 122 family, yet realized here in a quasi-one-dimensional Mott system. These findings highlight the central role of magnetoelastic coupling in iron-based superconductors beyond the itinerant regime.

I. INTRODUCTION

Iron-based compounds with strongly correlated electrons and magnetic order have been an active area of research for the past few decades. This field, was ignited by the 2008 discovery of superconductivity at high-temperatures in the LaO_{1-x}F_xFeAs compound ($T_c = 26$ K at ambient pressure [1] and 43 K under 4 GPa [2]). Since then T_c above 100 K was observed in a monolayer film of FeSe on a doped-SrTiO₃ substrate [3]. On top of superconductivity the iron-based compounds have been shown to display rich phase diagrams with various magnetic orders [4], orbital orders [5, 6], nematicity [7], multiferroicity [8], etc.

Recently the spin-ladder BaFe₂X₃ (X = S, Se) family was shown to exhibit both quasi-1D-superconductivity under pressure (T_c between 10 K and 26 K under 9 – 26 GPa [9–11]) and multiferroicity [8].

BaFe₂X₃ compounds are composed of one-dimensional ladders of edge-sharing Fe²⁺(X²⁻)₄ tetrahedra separated by Ba²⁺ ions. While the BaFe₂Se₃ compound exhibits an unconventional square-block antiferromagnetic (AFM) order [12], the BaFe₂S₃ one presents AFM stripes [9, 13, 14] (see Fig. 1). Under pressure these

Mott insulators turn metallic and then superconducting [9, 15, 16].

Both the BaFe₂S₃ and BaFe₂Se₃ compounds had been initially characterized, by standard X-ray diffraction, as centrosymmetric under ambient conditions [17]. However, recent pieces of work, high-resolution X-ray diffraction [8] and combination of theoretical DFT calculations with Infra-Red (IR) spectroscopy [18], revealed that BaFe₂Se₃ exhibits weak polar distortions and crystallizes in a non-centrosymmetric space group even at room temperature. As the system is cooled down this ferroelectric phase coexists with the magnetically ordered phase giving rise to multiferroicity.

The BaFe₂S₃ compound was first reported to belong to the *Cmcm* space group over the whole temperature range [19]. Recently however high-resolution X-ray experiments reported a structural phase transition at $T_S = 130$ K. In addition weak polar distortions were discovered over the whole temperature range. The room temperature space group was established to be *Cm2m*, and the low temperature one ($T < T_S$) to be *Pb2₁m* [20]. In this sample the magnetic transition sets up at $T_N = 95$ K [20] and does not seem to be associated with a structural change. A weak resistivity anomaly was also reported around $T^* = 180$ K [10, 13], attributed by the authors to an orbital ordering, and once more not associated to structural change. For sake of completeness one should mention that some authors also claimed the existence of a spin-glass phase below $T_G = 25$ K [21], this phase was

* These authors contributed equally to this work.

† Corresponding author: Marie-Bernadette.Lepetit@neel.cnrs.fr

‡ Corresponding author: victor.baledent@universite-paris-saclay.fr

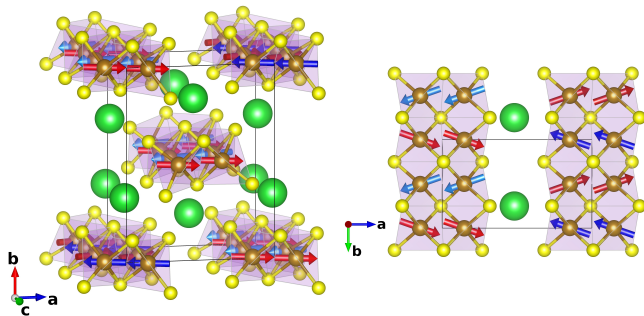


FIG. 1. Schematic picture of the atomic and magnetic structure of BaFe_2S_3 . The axes follow the $Cmcm$ setting. Ba: green, Fe: brown, S: yellow. The arrows show the magnetic moments on different Fe sites.

however never confirmed by other groups.

As lattice dynamics is well known to be a very thorough test of the symmetry of a compound, even more effective than high-resolution X-ray diffraction to decipher weak symmetry breaking, we will conduct in this paper a lattice dynamics study of BaFe_2S_3 , combining IR measurements and Density Functional Theory (DFT) phonons calculations.

At this point one should cite that the only available low-temperature lattice dynamics study of BaFe_2S_3 claims the later to be centrosymmetric with $Cmcm$ space group. This work is based on a combined Raman spectroscopy and non-magnetic DFT calculation of the phonon modes [22] using the PBE functional. As mentioned above the $Cmcm$ space group has already been outdated. Let us point out that the non-magnetic DFT-PBE calculation exhibits a metallic behavior. In addition it is well known that the PBE functional have a tendency to over-delocalization. As a consequence one can expect that the overlook of the magnetic ordering and the use of the PBE functional will prevent the possibility to decipher weak symmetry breakings (such as the $Cmcm$ versus $Cm2m$ symmetry breaking experimentally observed at room temperature in BaFe_2S_3 [20]).

II. METHODS

A. Single Crystal Sample Synthesis

BaFe_2S_3 single crystals were grown from the melt using a self-flux method [23]. Stoichiometric amounts of BaS (99.9%), Fe (99.9%), and S (99.999%) powders were mixed in a BaS:Fe:S molar ratio of 1:2.05:3. Approximately 2g of the mixture were pelletized, placed in a carbon crucible, and sealed in an evacuated quartz ampoule backfilled with a partial pressure of 300 mbar of argon.

The ampoule was heated in a vertical tubular furnace to 1100 °C and held at this temperature for 24 h to ensure homogenization. It was then slowly cooled to 750 °C at

a rate of 6 °C/h, followed by furnace cooling to room temperature. This procedure yielded a centimeter-sized pellet composed of densely packed, millimeter-sized rod-shaped crystals naturally co-aligned along the \vec{c} axis of the orthorhombic $Cmcm$ structure (ladder-leg direction).

The crystalline quality and bulk properties of these samples were thoroughly characterized in a previous study, confirming their high structural and chemical homogeneity [20].

B. Polarized Infrared Measurements

Millimeter-sized single crystals were selected and pre-oriented using X-ray diffraction at the Laboratoire de Physique des Solides. The crystals were mounted on a copper sample holder using silver paste to ensure optimal thermal contact. Particular care was taken to orient the samples such that the incident electric and magnetic field components were well defined with respect to the three crystallographic axes of the $Cmcm$ structure.

Infrared reflectivity measurements were performed at the AILES beamline of the SOLEIL synchrotron using a Bruker IFS125 Michelson interferometer. The experimental setup included a closed-cycle helium cryostat, a 4.2 K bolometer detector, and a 6 μm beamsplitter, providing a spectral resolution of 3 cm^{-1} . The incident radiation was linearly polarized using a polyethylene polarizer. Reflectivity spectra were collected in the temperature range 20–300 K. Absolute reflectivity was determined using an in situ gold evaporation technique, enabling accurate reference measurements.

C. Inelastic Neutron Scattering

Inelastic neutron scattering experiments were carried out on the cold-neutron triple-axis spectrometer THALES at the Institut Laue-Langevin (ILL) [24]. A pyrolytic graphite (PG) monochromator and analyzer were used. The sample temperature was controlled between 150 K and 10 K using a standard orange helium-flow cryostat.

The final neutron wave vector was fixed to $k_f = 1.5 \text{ \AA}^{-1}$, providing an optimal compromise between neutron flux and energy resolution (better than 50 μeV). The data were indexed in the orthorhombic $Cmcm$ setting with lattice parameters $a = 8.75 \text{ \AA}$ (rung direction), $b = 11.19 \text{ \AA}$ (perpendicular to the ladder plane), and $c = 5.28 \text{ \AA}$ (ladder-leg direction).

A single-crystal of approximately 0.5 cm^3 was aligned in the (H, H, L) scattering plane defined by the reciprocal lattice vectors $(H, H, 0)$ and $(0, 0, L)$. Owing to the reduced value of the neutron wave vector, only a limited number of magnetic Bragg reflections were accessible; all measurements were therefore performed at the $(1/2, 1/2, 1)$ position. The magnetic Bragg peaks exhibit a

mosaic spread comparable to that of the nuclear (1, 1, 0) and (2, 0, 0) reflections.

D. Theoretical Calculations

The *ab-initio* calculations were performed using DFT. In order to best account for self-interaction, we used the hybrid B3LYP functional [25] and a localized basis set. An all-electrons atomic gaussian basis set of $3\zeta + P$ quality was used for the Fe and S atoms [26]. The Ba atoms were represented using a relativistic core pseudopotential of the Stuttgart group (ECP46MWB [27]) and the associated basis set where the diffuse functions exponents were taken as 1.2 as recommended by Scuse-ria *et. al* [28]. The calculations were done using the CRYSTAL23 code [29]. The shrinking factor was set so that to sample the Brillouin zone with an approximate grid of $0.016 \pm 0.002 \text{ \AA}^{-1}$ intervals in each direction. The stripe-like spin order found in neutron scattering experiments [13, 14] was used in all calculations, geometry optimization as well as lattice dynamics.

III. RESULTS

A. Lattice Dynamics

1. Polarized Infrared spectroscopy

We measured the reflectance in the far-infrared range, with the electric field \vec{E} applied in all three $Cmcm$ lattice directions. Let us note that in this paper we will always refer to the $Cmcm$ axes, where \vec{a} is the ladder-rung direction, \vec{c} is the ladder-leg direction and \vec{b} is perpendicular to the ladders.

Fig. 2 shows the reflectance spectra measured at 300 K (red) and 20 K (blue), together with the corresponding heat maps illustrating the evolution of the phonon energies and intensities as a function of temperature. We used the Drude-Lorentz model to analyze the dielectric function. The details of the experimental fit can be found in the Supplementary Information (SI). The typical errors on the phonon frequencies, combining experimental resolution and fit uncertainty, are estimated to be smaller than 3 cm^{-1} .

2. First-principle Calculations & Symmetry Analysis

We first performed the Γ -point lattice dynamic calculations, after full geometry optimization, for the two space group cited in the literature for the low temperature phase, namely $Cmcm$ [17] and $Pb2_1m$ [20]. The total energy of the system was found to be 2.79 eV/f.u. lower for the $Pb2_1m$ group, in agreement with the recent X-ray results of Ref. 20.

Lattice dynamics calculation, at the Γ point, under harmonic approximation, indicated that both phases can be dynamically stable, without any imaginary phonon modes. Symmetry analysis yields the following irreducible representations (irrep) for the optical modes

$$\begin{aligned}
 Cmcm & : \underbrace{4B_{1u} \oplus 5B_{2u} \oplus 4B_{3u}}_{\text{IR active}} \oplus \underbrace{5A_g \oplus 6B_{1g} \oplus 3B_{2g} \oplus 4B_{3g}}_{\text{Raman active}} \\
 Pb2_1m & : \underbrace{21A_1 \oplus 13B_1 \oplus 21B_2}_{\text{IR+Raman active}} \oplus \underbrace{14A_2}_{\text{Raman active}}
 \end{aligned}$$

Again the symmetry analysis discards the $Cmcm$ space group, as for instance it yields only $4B_{3u}$ modes when the light polarization is parallel to \vec{a} , while our IR experiment clearly sees 9 (see Fig. 2).

Table I displays the DFT phonons frequencies for the $Pb2_1m$ group and the best fit to the experimental values taking into account the light polarization. Several modes seen in the experiment cannot be assigned in the $Pb2_1m$ group. In both the B_2 and A_1 irreps the 312 cm^{-1} and 329 cm^{-1} modes, seen in both polarization, cannot be simultaneously assigned. In the B_1 irrep, the 329 cm^{-1} and 404 cm^{-1} modes do not have DFT counterparts.

TABLE I. DFT frequencies (cm^{-1}) of optical phonons in the $Pb2_1m$ space group and assignment of the IR modes measured at 20 K. The experimental modes typeset in red cannot be assigned to the computed ones, either because there is only one theoretical mode for two experimental ones, or because there is no theoretical mode computed in the energy range.

DFT	IR	DFT	IR	DFT	IR
B_2	$\vec{E} \parallel \vec{a}$	A_1	$\vec{E} \parallel \vec{b}$	B_1	$\vec{E} \parallel \vec{c}$
47.5		21.1		39.7	
51.5		54.5		44.7	
71.4		57.0		82.7	79
78.4		71.9		91.9	
89.5	84	81.0		100.5	
93.8	93	85.3	95	122.0	117
122.8	124	116.0	124	130.2	
130.5		133.1		230.2	
137.8		135.4		241.8	
139.9	144	147.3	145	250.9	
182.5	183	169.2		266.2	
198.9		192.7		283.0	
204.2		213.5		287.1	
250.4		245.4			329
269.9		276.1			404
272.9		276.3			
280.5		283.8			
320.4	312	324.5	312		
	329		329		
354.4	349	346.2	355		
378.5		365.2			
402.9	404	379.4			
					404

The fact that several modes are seen with different light polarization claims for a symmetry lowering. We

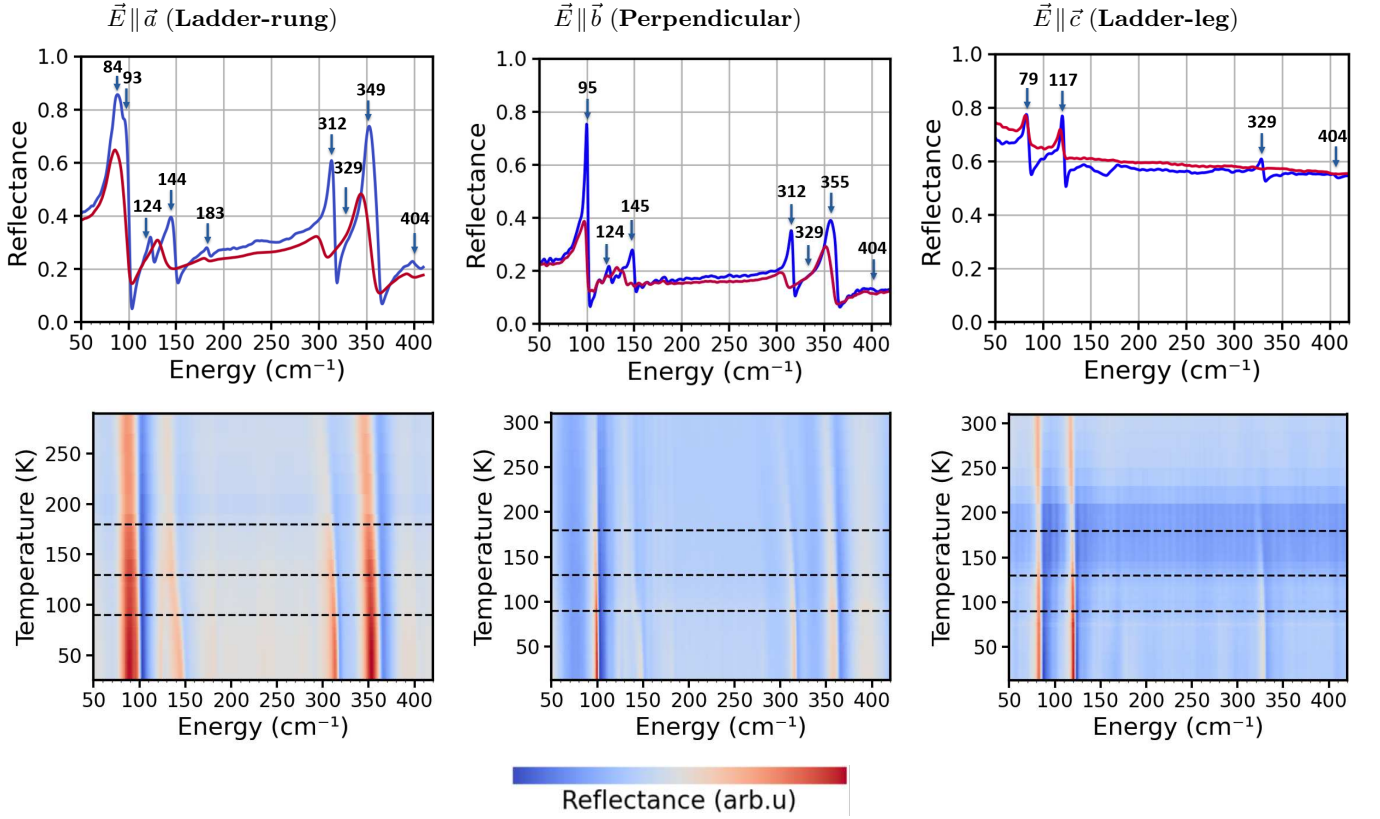


FIG. 2. **Temperature-dependent reflectance spectra.** (Top row) Reflectance measured at room temperature (red) and at the lowest accessible temperature 20 K (blue), with the electric field \vec{E} applied along the three crystallographic directions of the $Cmcm$ space group. The arrows mark the fitted IR-active phonon modes at 20 K. (Bottom row) Heat maps showing the evolution of the reflectance as a function of temperature for the three directions, after background subtraction. Horizontal dashed lines, marking T_N , T_S , and T^* in ascending order, are added to guide the eye. The reflectance intensity (in arbitrary unit) scales from low (blue) to high (red).

thus investigated the lattice dynamics for all maximal subgroups of $Pb2_1m$, i.e. $P2_1$, Pm and Pc . Symmetry analysis of the irrep conjunction tells us that

$$Pm: \quad A' = A_1 \oplus B_2 = (A_g \oplus B_{2u}) \oplus (B_{1g} \oplus B_{3u}) \\ A'' = B_1 \oplus A_2 = (B_{3g} \oplus B_{1u}) \oplus (B_{2g} \oplus A_u)$$

$$Pc: \quad A' = A_1 \oplus B_1 = (A_g \oplus B_{2u}) \oplus (B_{3g} \oplus B_{1u}) \\ A'' = A_2 \oplus B_2 = (B_{2g} \oplus A_u) \oplus (B_{1g} \oplus B_{3u})$$

$$P2_1: \quad A = A_1 \oplus A_2 = (A_g \oplus B_{2u}) \oplus (B_{2g} \oplus A_u) \\ B = B_1 \oplus B_2 = (B_{3g} \oplus B_{1u}) \oplus (B_{1g} \oplus B_{3u})$$

At this point one shall remember that the light polarisation along the \vec{a} $Cmcm$ axis addresses phonons in the B_{3u} irrep, the polarisation along \vec{b} addresses phonons in the B_{2u} irrep and along \vec{c} addresses phonons in the B_{1u} irrep. Our calculations in those three groups yield similar formation energies as in the $Pb2_1m$ group, thus not allowing to discriminate between them. This is consistent with the fact that diffraction experiment was not able to determine the exact structure. Going now to the lattice dynamics, unfortunately none of the three subgroups

could account for all the observed phonons modes when placed in the proper irreps (see SI for detailed tables).

We thus finally performed phonon calculation within the $P1$ space group. The results are displayed in Table II. In order to better assign the phonons we looked whether the main atomic displacements are compatible with the light polarisation direction. This time all modes can easily be accounted for. The lattice dynamics analysis thus points toward the loss of all point group symmetry operations.

3. Evolution of phonons with respect to temperature

Looking at the temperature dependence of the phonon modes, one can see that several phonons (at 145 cm⁻¹, 312 cm⁻¹ and 355 cm⁻¹) exhibit anomalies in their intensities at the magnetic transition (see Fig. 3). This observation clearly points toward the existence of magneto-elastic coupling. These phonons are seen when the light polarisation is either along the \vec{a} or \vec{b} . The temperature anomaly is larger when the light polarization is perpendicular to the ladders (along \vec{b}), in agreement with the

TABLE II. DFT frequencies (cm^{-1}) of optical phonons computed in $P1$ and their best experimental assignment.

DFT		IR			DFT		IR		
A	$\vec{E} \parallel \vec{a}$	$\vec{E} \parallel \vec{b}$	$\vec{E} \parallel \vec{c}$	A	$\vec{E} \parallel \vec{a}$	$\vec{E} \parallel \vec{b}$	$\vec{E} \parallel \vec{c}$	$\vec{E} \parallel \vec{c}$	
72.1				136.8					
75.2	84			136.8					
81.8				144.1	144	145			
84.9		95		151.6					
87.5				156.9					
93.3			79	168.3					
94.8				170.7	183				
96.2				199.7					
97.1	93			200.0					
98.0				202.7					
102.8								
109.1				296.7					
110.0		117		318.5	312	312			
113.8				336.8	329	329	329		
117.3				346.4	349				
121.5	124			347.3		355			
122.4		124		378.9					
123.0				381.3					
135.8				383.2					
136.5				396.5	404	404	404		

fact that the interladder couplings (responsible for the long-range 3D-ordering) are much weaker than the intraladder ones.

Above the structural transition, T_S , three phonons disappear i.e. the phonon seen at 93cm^{-1} (see SI) and 124cm^{-1} when the light polarisation is along \vec{a} (ladder rungs) and the phonon seen at 124cm^{-1} when the light polarisation is along the \vec{b} direction. In addition, the phonon at 145cm^{-1} exhibit anomalies at T_S but its intensity does not dies out above T_S .

Let us look now at the displacement vectors of the two modes at 124cm^{-1} (see SI for figures). The first mode seen when $\vec{E} \parallel \vec{a}$ mainly involves Fe movements along the ladder rungs. The second one, seen when $\vec{E} \parallel \vec{b}$, mainly involves movements of the sulfur atoms along the ladder legs. These two modes should thus be coupled to the ladder-rung and ladder-leg magnetic-exchange interactions.

These intra-ladder interactions are expected to be much larger than the inter-ladder ones. As the ladders are responsible for the magnetic transition at T_N , one can expect the existence of intra-ladder short-range magnetic correlations above T_N . In view of those two observations one can wonder whether the structural transition at T_S could originate from the intra-ladder short-range magnetic correlations.

In order to confirm this hypothesis we performed neutrons scattering to study the behavior of magnetic Bragg's peaks through the two phase transitions.

B. Magnetic Fluctuations

To investigate the magnetic fluctuations and extract the associated correlation lengths, we performed momentum (\mathbf{Q}) and energy ($\hbar\omega$) scans around the magnetic Bragg position $\mathbf{Q} = (\frac{1}{2}, \frac{1}{2}, 1)$. Momentum scans were carried out both along the ladder direction, i.e. $(\frac{1}{2}, \frac{1}{2}, L)$, and perpendicular to it by simultaneously varying the H and K components along $(H, H, 1)$. In the following, these measurements are referred to as L , HH , and E scans, respectively. All measurements were performed under identical experimental conditions over the temperature range $10\text{ K} \leq T \leq 140\text{ K}$.

The peaks were fitted using pseudo-Voigt functions along each direction (see Supplemental Information for details). At the lowest temperature ($T=10\text{ K}$), the energy linewidth is resolution-limited, with a full width at half maximum (FWHM) of $44\ \mu\text{eV}$, corresponding to the instrumental resolution. The maximum intensities extracted from the three types of scans are plotted as a function of temperature in the top panel of Fig. 4. Within experimental uncertainty, the intensity and its temperature dependence are independent of the scan direction.

The temperature evolution of the FWHM along the ladder direction, perpendicular to the ladder, and in energy is shown in the bottom panel of Fig. 4. At low temperatures and up to $T_N \approx 95\text{ K}$, the widths remain constant. The \mathbf{Q} -widths are limited by the crystal mosaicity, with a slightly narrower width along the ladder direction, consistent with the quasi-one-dimensional character of the system and previous reports on parent compounds BaFe_2Se_3 [30]. The energy width remains limited by the instrumental resolution ($44\ \mu\text{eV}$).

Above T_N , a progressive broadening is observed in both momentum and energy. The increase of the \mathbf{Q} -width indicates a reduction of the magnetic correlation lengths along and perpendicular to the ladder direction, while the broadening in energy reflects a shortening of the magnetic fluctuation lifetime. The magnetic signal becomes undetectable above $T_S \approx 125\text{--}130\text{ K}$, suggesting that the magnetic correlations are no longer spatially coherent in reciprocal space and that the associated spectral weight is distributed over a broad momentum range and thus is assimilated as a homogenous background component.

Overall, these inelastic neutron scattering results demonstrate that the magnetic order is three-dimensional, long-ranged, and static below T_N . Between T_N and T_S , the system exhibits short-range, three-dimensional dynamic correlations (and not one-dimensional as expected), and above T_S no measurable three-dimensional magnetic correlations are detected.

IV. CONCLUSION

In this work, we combined polarized synchrotron infrared spectroscopy, hybrid-functional DFT lattice-

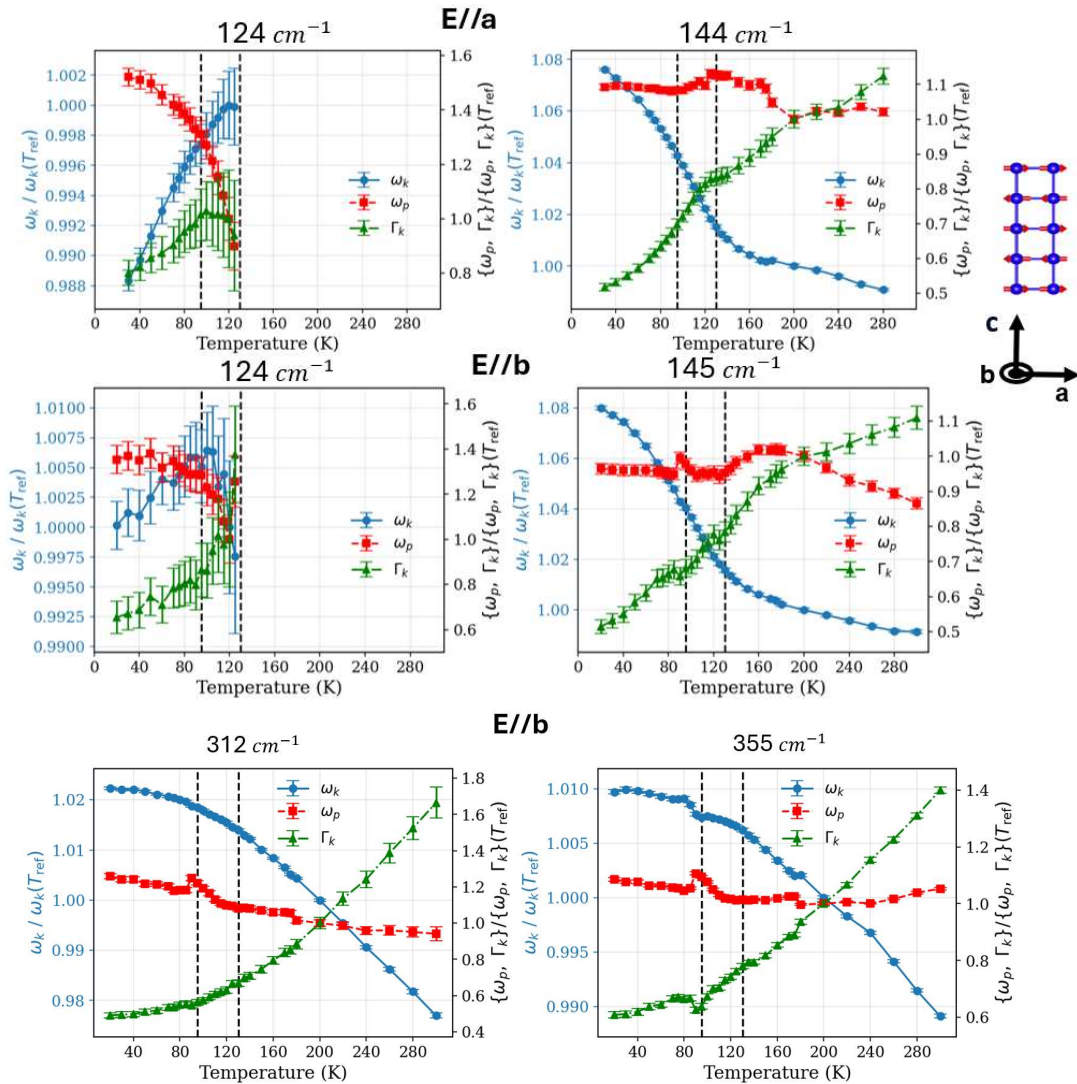


FIG. 3. Temperature evolution of the 124 cm^{-1} , e 145 cm^{-1} , 312 cm^{-1} and 355 cm^{-1} phonons modes. The two 124 cm^{-1} modes disappear at T_S . Blue curves : oscillator frequencies, ω_k . Red curves : normalized plasma frequencies, ω_p . Green curves : width, Γ_k .

dynamics calculations, and inelastic neutron scattering to elucidate the interplay between structure, lattice dynamics, and magnetism to reveal the ground state of BaFe_2S_3 .

First, the symmetry analysis of the infrared-active phonons, supported by first-principles calculations, demonstrates that the crystal symmetry is lower than the previously proposed $Pb2_1m$ space group and is consistent with a $P1$ description at low temperature. The loss of residual point-group symmetry operations is required to account for the full set of experimentally observed phonon modes and their polarization dependence. Second, neutron scattering establishes that below $T_N \approx 95 \text{ K}$ the magnetic order is three-dimensional, long-ranged, and static. Between T_N and $T_S \approx 125\text{--}130 \text{ K}$, the system exhibits three-dimensional, short-range dynamic magnetic correlations, as evidenced by the simultaneous broadening in momentum and energy. Above T_S ,

no measurable magnetic correlations persist in reciprocal space. Third, the temperature evolution of selected phonon modes reveals clear anomalies at both T_N and T_S . The modes affected at T_S predominantly involve either Fe or S atomic displacements. These motions modulate the Fe-Fe exchange paths along the rungs and legs of the ladders. The anomalies at T_N reflect magnetoelastic coupling associated with the onset of static long-range magnetic order, whereas the anomalies at T_S occur precisely at the temperature where magnetic fluctuations first become detectable in neutron scattering.

These results establish a direct link between the emergence of magnetic fluctuations and the structural transition. Importantly, although the ladder geometry and previous study [30] suggests dominant intra-ladder exchange interactions, our neutron data demonstrate that the fluctuations between T_N and T_S retain a three-

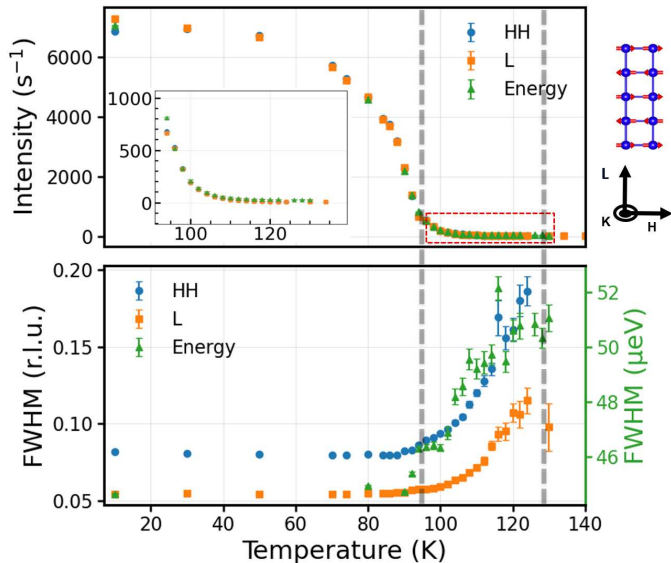


FIG. 4. **Neutron scattering.** maximum intensity, A of eq. 2 in SI (top) and FWHM (bottom) evolutions as a function of temperature for HH , L and E scans around the magnetic Bragg peak $(\frac{1}{2}, \frac{1}{2}, 1)$. Vertical gray dashed lines mark T_N and T_S , respectively. Inset in top panel displays a zoom in for $T_N \leq T \leq T_S$

T (K)	Our previous work		This work		
	Literature	Neutron diffraction	X-ray diffraction	Infrared spectroscopy	Inelastic neutron scattering
300 K	$Cmcm$	PM	$Cm2m$	$Cm2m$ compatible	PM
$T_S \approx 130$ K					Short range dynamic fluctuations
$T_N \approx 95$ K	Collinear Stripe AFM	P_qm Non-collinear Stripe AFM	$Pb2_1m$	$P1$	Static Long range order

FIG. 5. Summary of the multi-technique ambient pressure temperature-dependent results. The diagram compares the structural and magnetic information extracted from x-ray diffraction, neutron diffraction (same group previous work), infrared spectroscopy and inelastic neutron scattering (from this work) and contrasts them with the literature consensus [9, 31, 32].

dimensional character: finite correlation lengths are observed both along and perpendicular to the ladder direction. Thus, the structural transition at T_S coincides not with static magnetic order, but with the onset of three-dimensional dynamic magnetic correlations. This indicates that short-range, dynamical magnetic fluctuations seem sufficient to drive a static structural instability.

This phenomenology is reminiscent of the iron-

pnictide 122 family, in particular $BaFe_2As_2$, where a tetragonal-to-orthorhombic structural transition occurs at or slightly above the stripe-type antiferromagnetic ordering temperature [33]. In that case, extensive experimental [34–36] and theoretical work [37–39] has established that the structural distortion is electronically driven and closely tied to spin-driven nematic fluctuations in these families. In $BaFe_2As_2$, the structural transition lowers the symmetry prior to or concomitantly with long-range magnetic order, and is widely interpreted as arising from a magnetic (or spin-nematic) instability of the electronic system.

The situation in $BaFe_2S_3$ shares key similarities but also important differences. As in the 122 pnictides, the structural transition precedes the establishment of static long-range magnetic order and coincides with the onset of magnetic correlations. However, unlike $BaFe_2As_2$, where the instability is often described in terms of electronic nematic order in an itinerant metallic system, $BaFe_2S_3$ is described as a Mott insulator with a quasi-one-dimensional ladder structure, with no electronic nematicity breaking the four-fold symmetry, absent in this case. Here, the structural transition occurs in a regime where magnetic correlations are already three-dimensional but remain dynamic and short-ranged. This suggests that, in $BaFe_2S_3$, magnetoelastic coupling associated with correlated local moments — rather than an itinerant electronic instability — is the primary driving mechanism of the symmetry lowering.

Therefore, $BaFe_2S_3$ provides a distinct realization of magnetically driven structural instability: short-range, dynamic, yet three-dimensionally correlated magnetic fluctuations can stabilize a static structural distortion. This highlights the robustness of magnetically mediated lattice instabilities across very different electronic regimes — from itinerant pnictides to quasi-one-dimensional Mott ladder systems — and underscores the central role of magnetoelastic coupling in shaping the phase diagrams of iron-based superconductors.

V. ACKNOWLEDGMENT

We acknowledge the MORPHEUS platform at the Laboratoire de Physique des Solides for sample orientation and alignment. We acknowledge SOLEIL for providing the synchrotron beamtime (proposals : 20230487,20242024) and ILL the neutron beamtime (DOI: 10.5291/ILL-DATA.4-03-1780). M.-B.L. and S.D. acknowledge the IDRIS high-performance computer center for the calculation time under the GENCI project n°0801842. This work was financially supported by the ANR COCOM 20-CE30-0029, the France 2030 programme ANR-11-IDEX-0003 via Integrative Institute of Materials from Paris-Saclay University - 2IM@UPSaclay, the Paris Ile-de-France Region in the framework of DIM MaTerRE (project DAC-VX).

- [1] Y. Kamihara, T. Watanabe, M. Hirano, and H. Hosono, Iron-Based Layered Superconductor $\text{La}[\text{O}_{1-x}\text{F}_x]\text{FeAs}$ ($x=0.05-0.12$) with $T_c = 26$ K, *J. Am. Chem. Soc.* **130**, 3296 (2008).
- [2] H. Takahashi, K. Igawa, K. Arii, Y. Kamihara, M. Hirano, and H. Hosono, Superconductivity at 43 K in an iron-based layered compound $\text{LaO}_{1-x}\text{F}_x\text{FeAs}$, *Nature* **453**, 376 (2008).
- [3] J.-F. Ge, Z.-L. Liu, C. Liu, C.-L. Gao, D. Qian, Q.-K. Xue, Y. Liu, and J.-F. Jia, Superconductivity in single-layer films of FeSe with a transition temperature above 100 K, *Nature Mater.* **14**, 285 (2015).
- [4] P. Dai, Antiferromagnetic order and spin dynamics in iron-based superconductors, *Rev. Mod. Phys.* **87**, 855 (2015).
- [5] N. D. Patel, A. Nocera, G. Alvarez, A. Moreo, S. Johnston, and E. Dagotto, Fingerprints of an orbital-selective Mott phase in the block magnetic state of BaFe_2Se_3 ladders, *Commun. Phys.* **2**, 64 (2019).
- [6] S. Hosoi, T. Aoyama, K. Ishida, Y. Mizukami, K. Hashizume, S. Imaizumi, Y. Imai, K. Ohgushi, Y. Nambu, M. Kimata, S. Kimura, and T. Shibauchi, Dichotomy between orbital and magnetic nematic instabilities in BaFe_2S_3 , *Phys. Rev. Research* **2**, 043293 (2020).
- [7] A. E. Böhrer, J.-H. Chu, S. Lederer, and M. Yi, Nematicity and nematic fluctuations in iron-based superconductors, *Nat. Phys.* **18**, 1412 (2022).
- [8] W. Zheng, V. Balédent, M. B. Lepetit, P. Retailleau, E. V. Elslande, C. R. Pasquier, P. Auban-Senzier, A. Forget, D. Colson, and P. Foury-Leylekian, Room temperature polar structure and multiferroicity in BaFe_2Se_3 , *Phys. Rev. B* **101**, 020101 (2020).
- [9] H. Takahashi, A. Sugimoto, Y. Nambu, T. Yamauchi, Y. Hirata, T. Kawakami, M. Avdeev, K. Matsubayashi, F. Du, C. Kawashima, H. Soeda, S. Nakano, Y. Uwatoko, Y. Ueda, T. J. Sato, and K. Ohgushi, Pressure-induced superconductivity in the iron-based ladder material BaFe_2S_3 , *Nat. Mater.* **14**, 1008 (2015).
- [10] T. Yamauchi, Y. Hirata, Y. Ueda, and K. Ohgushi, Pressure-Induced Mott Transition Followed by a 24-K Superconducting Phase in BaFe_2S_3 , *Phys. Rev. Lett.* **115**, 246402 (2015).
- [11] J. Ying, H. Lei, C. Petrovic, Y. Xiao, and V. V. Struzhkin, Interplay of magnetism and superconductivity in the compressed fe-ladder compound bafe_2se_3 , *Physical Review B* **95**, 241109 (2017).
- [12] J. M. Caron, J. R. Neilson, D. C. Miller, A. Llobet, and T. M. McQueen, Iron displacements and magnetoelastic coupling in the antiferromagnetic spin-ladder compound bafe_2se_3 , *Phys. Rev. B* **84**, 180409 (2011).
- [13] Y. Hirata, S. Maki, J. I. Yamaura, T. Yamauchi, and K. Ohgushi, Effects of stoichiometry and substitution in quasi-one-dimensional iron chalcogenide BaFe_2S_3 , *Phys. Rev. B* **92**, 205109 (2015).
- [14] Y. T. Chan, S. Roh, S. Shin, T. Park, M. Dressel, and E. Uykur, Three-dimensional hopping conduction triggered by magnetic ordering in the quasi-one-dimensional iron-ladder compounds BaFe_2S_3 and BaFe_2Se_3 , *Phys. Rev. B* **102**, 035120 (2020).
- [15] S. Chi, Y. Uwatoko, H. Cao, Y. Hirata, K. Hashizume, T. Aoyama, and K. Ohgushi, Magnetic Precursor of the Pressure-Induced Superconductivity in Fe-Ladder Compounds, *Phys. Rev. Lett.* **117**, 10.1103/PhysRevLett.117.047003 (2016).
- [16] P. Materne, W. Bi, J. Zhao, M. Y. Hu, M. L. Amigó, S. Seiro, S. Aswartham, B. Büchner, and E. E. Alp, Bandwidth controlled insulator-metal transition in BaFe_2S_3 : A Mössbauer study under pressure, *Phys. Rev. B* **99**, 10.1103/PhysRevB.99.020505 (2019).
- [17] H. Hong and H. Steinfink, The crystal chemistry of phases in the Ba-Fe-S and Se systems, *J. Solid State Chem.* **5**, 93 (1972).
- [18] M. J. Weseloh, V. Balédent, W. Zheng, M. Verseils, P. Roy, J. B. Brubach, D. Colson, A. Forget, P. Foury-Leylekian, and M.-B. Lepetit, Lattice dynamics of BaFe_2Se_3 , *Journal of Physics: Condensed Matter* **34**, 255402 (2022).
- [19] S. Wu, B. A. Frandsen, M. Wang, M. Yi, and R. Birgeneau, Iron-Based Chalcogenide Spin Ladder BaFe_2X_3 ($X = \text{Se}, \text{S}$), *J. Supercond. Nov. Magn.* **33**, 143 (2020).
- [20] Y. Oubaid, V. Balédent, O. Fabelo, L. Bocher, C. V. Colin, S. Chattopadhyay, E. Elkaim, M. Verseils, A. Forget, D. Colson, D. Bounoua, P. Fertey, and P. Foury-Leylekian, New insight on the properties of the superconducting iron spin ladder BaFe_2S_3 , *Frontiers of Physics* **21**, 055201 (2026).
- [21] Z. S. Gönen, P. Fournier, V. Smolyaninova, R. Greene, F. M. Araujo-Moreira, and B. Eichhorn, Magnetic and Transport Properties of $\text{Ba}_6\text{Fe}_8\text{S}_{15}$ and BaFe_2S_3 : Magnetoresistance in a Spin-Glass-Like Fe(II) System, *Chemistry of Materials* **12**, 3331 (2000).
- [22] Z. V. Popović, M. Šćepanović, N. Lazarević, M. Opačić, M. M. Radonjić, D. Tanasković, H. Lei, and C. Petrovic, Lattice dynamics of BaFe_2X_3 ($X = \text{S}, \text{Se}$) compounds, *Phys. Rev. B* **91**, 064303 (2015).
- [23] M. L. Amigó, Q. Stahl, A. Maljuk, A. U. B. Wolter, C. Hess, J. Geck, S. Wurmehl, S. Seiro, and B. Büchner, Revisiting the influence of Fe excess in the synthesis of BaFe_2S_3 , *Phys. Rev. Mater.* **5**, 094801 (2021).
- [24] V. Balédent, Y. Oubaid, and N. Dhami, Magnetic fluctuations in quasi 1d compound BaFe_2S_3 , *Institut Laue-Langevin (ILL)* 10.5291/ILL-DATA.4-03-1780 (2025).
- [25] A. D. Becke, Density-functional thermochemistry. iii. the role of exact exchange, *J. Chem. Phys.* **98**, 5648 (1993).
- [26] D. Vilela Oliveira, J. Laun, M. F. Peintinger, and T. Bredow, Bsse-correction scheme for consistent gaussian basis sets of double-and triple-zeta valence with polarization quality for solid-state calculations, *J. Comput. Chem.* **40**, 2364 (2019).
- [27] M. Kaupp, P. v. R. Schleyer, H. Stoll, and H. Preuss, Pseudopotential approaches to Ca, Sr, and Ba hydrides. Why are some alkaline earth MX_2 compounds bent?, *J. Chem. Phys.* **94**, 1360 (1991).
- [28] J. Heyd, J. E. Peralta, G. E. Scuseria, and R. L. Martin, Energy band gaps and lattice parameters evaluated with the heyd-scuseria-ernzerhof screened hybrid functional, *J. Chem. Phys.* **123**, 10.1063/1.2085170 (2005).
- [29] A. Erba, J. K. Desmarais, S. Casassa, B. Civalleri, L. Donà, I. J. Bush, B. Searle, L. Maschio, L. Edith-Daga, A. Cossard, C. Ribaldone, E. Ascrizzi, N. L. Marana, J.-P. Flament, and B. Kirtman, Crystal23: A program for computational solid state physics and chemistry, *J.*

- Chem. Theory Comput.* **19**, 6891 (2022).
- [30] A. Roll, S. Petit, A. Forget, D. Colson, A. Banerjee, P. Foury-Leleykian, and V. Balédent, Purely antiferromagnetic frustrated Heisenberg model in the spin-ladder compound BaFe_2Se_3 , *Phys. Rev. B* **108**, 014416 (2023).
- [31] L. Zheng, B. A. Frandsen, C. Wu, M. Yi, S. Wu, Q. Huang, E. Bourret-Courchesne, G. Simutis, R. Khasanov, D.-X. Yao, M. Wang, and R. J. Birgeneau, Gradual enhancement of stripe-type antiferromagnetism in the spin-ladder material BaFe_2S_3 under pressure, *Phys. Rev. B* **98**, 180402 (2018).
- [32] S. Imaizumi, T. Aoyama, R. Kimura, K. Sasaki, Y. Nambu, M. Avdeev, Y. Hirata, Y. Ikemoto, T. Moriwaki, Y. Imai, *et al.*, Structural, electrical, magnetic, and optical properties of iron-based ladder compounds $\text{BaFe}_2(\text{S}_{1-x}\text{Se}_x)_3$, *Physical Review B* **102**, 035104 (2020).
- [33] M. G. Kim, R. M. Fernandes, A. Kreyssig, J. W. Kim, A. Thaler, S. L. Bud'ko, P. C. Canfield, R. J. McQueeney, J. Schmalian, and A. I. Goldman, Character of the structural and magnetic phase transitions in the parent and electron-doped BaFe_2As_2 compounds, *Physical Review B - Condensed Matter and Materials Physics* **83**, 10.1103/PhysRevB.83.134522 (2011).
- [34] S. A. J. Kimber, A. Kreyssig, Y.-Z. Zhang, H. O. Jeschke, R. Valenti, F. Yokaichiya, E. Colombier, J. Yan, T. C. Hansen, T. Chatterji, R. J. McQueeney, P. C. Canfield, and A. I. Goldman, Similarities between Structural Distortions under Pressure and Chemical Doping in Superconducting BaFe_2As_2 , *Nat. Mater.* **8**, 471 (2009).
- [35] Q. Huang, Y. Qiu, W. Bao, M. A. Green, J. W. Lynn, Y. C. Gasparovic, T. Wu, G. Wu, and X. H. Chen, Neutron-Diffraction Measurements of Magnetic Order and a Structural Transition in the Parent BaFe_2As_2 Compound of FeAs-Based High-Temperature Superconductors, *Phys. Rev. Lett.* **101**, 257003 (2008).
- [36] J. J. Wu, J. F. Lin, X. C. Wang, Q. Q. Liu, J. L. Zhu, Y. M. Xiao, P. Chow, and C. Q. Jin, Magnetic and structural transitions of SrFe_2As_2 at high pressure and low temperature, *Scientific Reports* **4**, 10.1038/srep03685 (2014).
- [37] C. Fang, H. Yao, W.-F. Tsai, J. Hu, and S. A. Kivelson, Theory of electron nematic order in LaFeAsO , *Physical Review B—Condensed Matter and Materials Physics* **77**, 224509 (2008).
- [38] R. M. Fernandes, L. H. Vanbeebber, S. Bhattacharya, P. Chandra, V. Keppens, D. Mandrus, M. A. McGuire, B. C. Sales, A. S. Sefat, and J. Schmalian, Effects of nematic fluctuations on the elastic properties of iron arsenide superconductors, *Phys. Rev. Lett.* **105**, 10.1103/PhysRevLett.105.157003 (2010).
- [39] R. M. Fernandes, A. V. Chubukov, and J. Schmalian, What drives nematic order in iron-based superconductors?, *Nat. Phys.* **10**, 97 (2014).

Supplemental Material (SM) for: “Ground State of BaFe₂S₃ from Lattice and Spin Dynamics”

CONTENTS

I. Infrared Spectroscopies and Phonon Modes Fitting	1
II. Lattice Dynamics Calculations	3
III. Phonon Temperature-dependence Anomalies and displacements	4
IV. Inelastic Neutron scattering	6
References	6

I. INFRARED SPECTROSCOPIES AND PHONON MODES FITTING

Experimental phonon frequencies were obtained by fitting the data using the usual Drude–Lorentz model for the dielectric function of insulating materials [1]. The dielectric function is thus expressed as the sum of harmonic oscillators, as described by the equation 1 :

$$\epsilon(\omega) = \epsilon_\infty + \sum_k \frac{\omega_{p,k}^2}{\omega_{0,k}^2 - \omega^2 - i\Gamma_k \omega} \quad (1)$$

where ϵ_∞ is the dielectric constant at infinite frequency, and $\omega_{0,k}$, $\omega_{p,k}$, and Γ_k represent respectively the oscillator frequency, plasma frequency and energy width of the k^{th} harmonic oscillator. The model parametrizes the complex permittivity as shown in the equation 1. To assess the quality of the fit we defined the goodness of fit (GOF) parameter quantified by :

$$\text{GOF} = 1 - \frac{\text{SS}_{\text{res}}}{\text{SS}_{\text{tot}}}, \quad \text{SS}_{\text{res}} = \sum_{i=1}^n (y_i - \epsilon(\omega_i))^2,$$

$$\text{SS}_{\text{tot}} = \sum_{i=1}^n (y_i - \bar{y})^2 \quad \text{with} \quad \bar{y} = \sum_{i=1}^n \frac{y_i}{n}$$

where, n is the number of measured points, y_i is the measured reflectance at ω_i , $\epsilon(\omega_i)$ is the Drude–Lorentz fit at ω_i (eq. 1).

The average value for the fits was around $\text{GOF} \approx 0.99$.

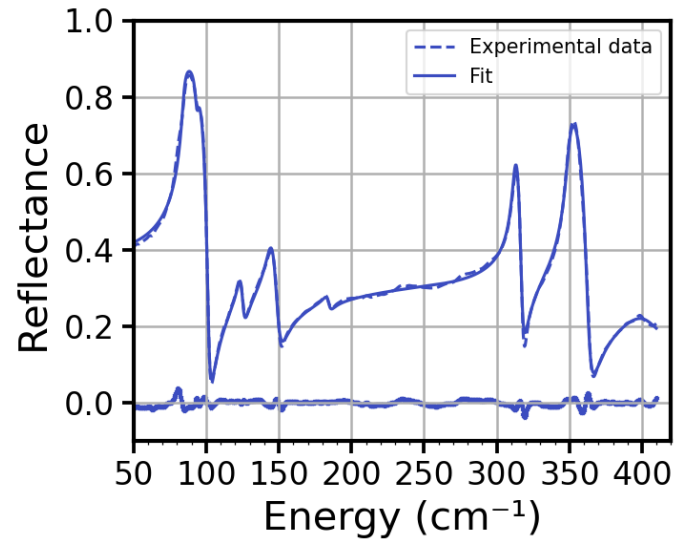


FIG. 1. Reflectance fitting using a Drude–Lorentz (DL) dielectric model. Measured reflectance in the rung direction of BaFe_2S_3 ($\mathbf{E} \parallel a$, 30 K; solid line) together with the DL fit (dashed). The residuals (data – fit) are shown in the same panel as a curve centered around zero.

III. PHONON TEMPERATURE-DEPENDENCE ANOMALIES AND DISPLACEMENTS

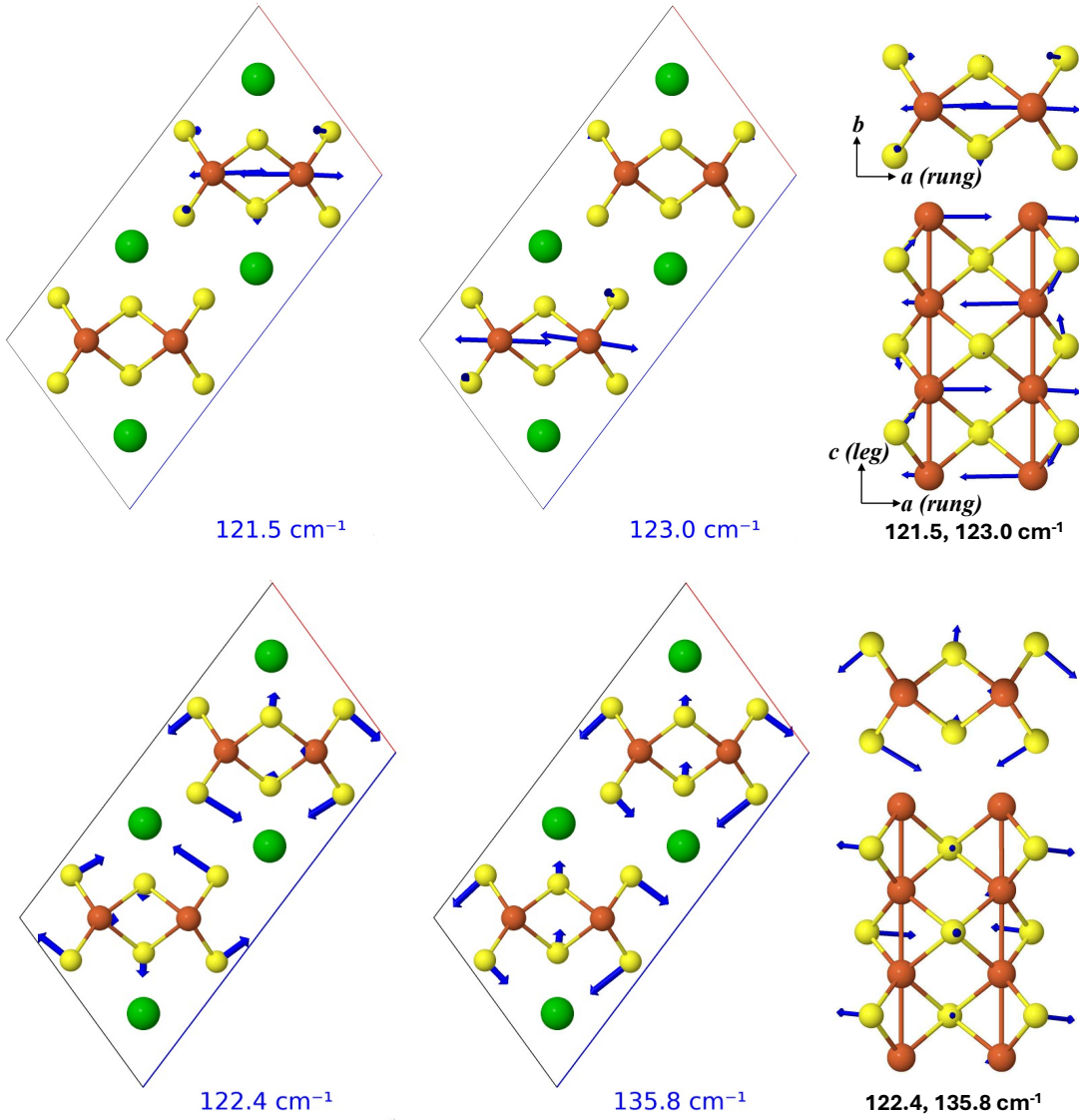


FIG. 2. Atomic displacement vectors for DFT-phonon modes associated with the two IR modes seen at 124 cm^{-1} , as well as their counterpart issued from the symmetry breaking.

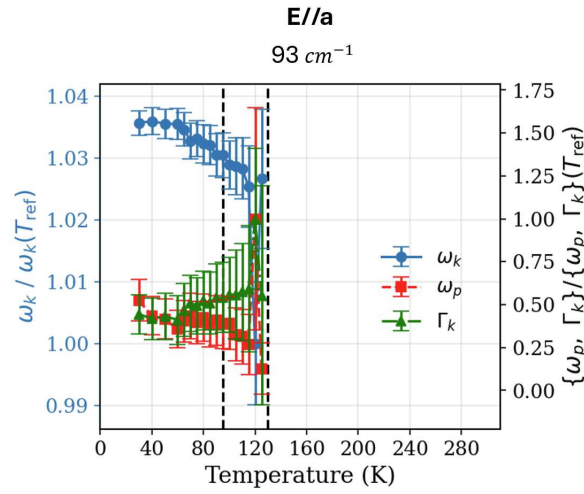


FIG. 3. Temperature dependence of the phonon seen at 93 cm^{-1} . Blue : oscillator frequencies, ω_k . Red : normalized plasma frequencies, ω_p . Green : width, Γ_k .

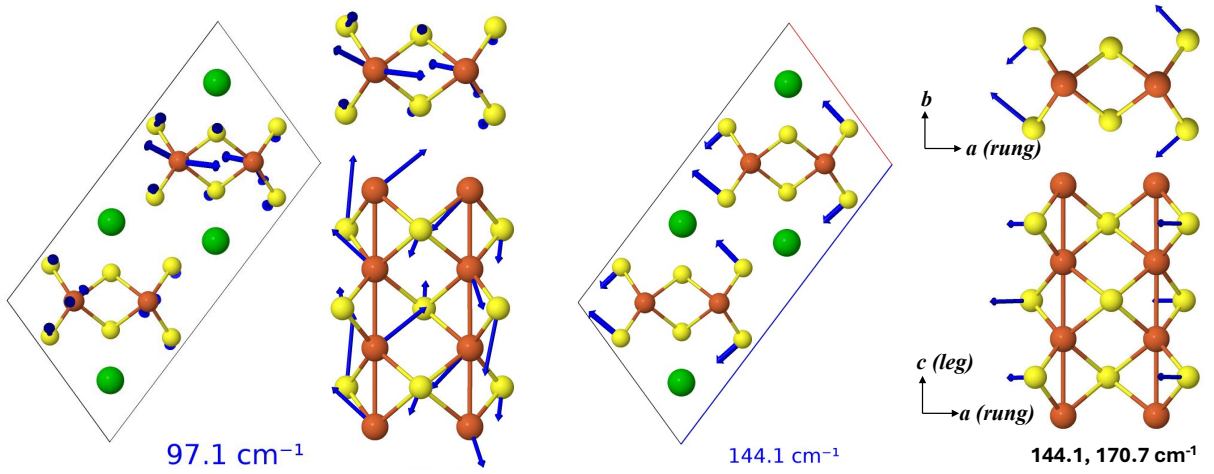


FIG. 4. Atomic displacement vectors for DFT-phonon mode, assigned with the 93 cm^{-1} IR mode (seen when $\vec{E} \parallel \vec{a}$), and the $144 \text{ cm}^{-1}/145 \text{ cm}^{-1}$ IR mode seen when the light polarisation is either along \vec{a} or \vec{b} .

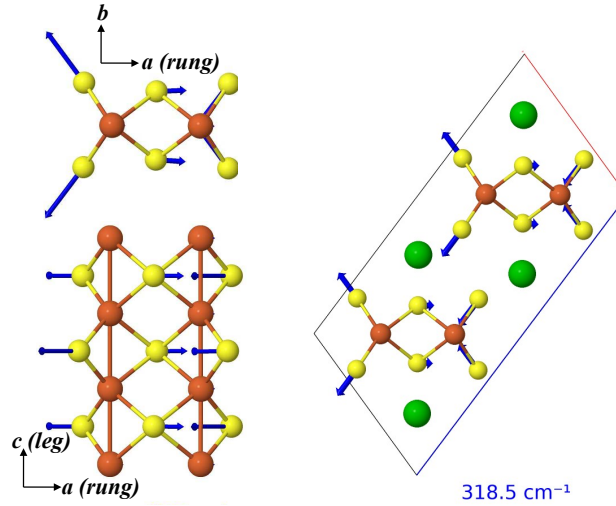


FIG. 5. Atomic displacement vectors for DFT-phonon modes associated with the IR 315 cm^{-1} mode.

IV. INELASTIC NEUTRON SCATTERING

Figure 6 summarizes neutron-scattering cuts acquired in the vicinity of the magnetic wave vector $\mathbf{Q}_{\text{mag}} \simeq (0.5, 0.5, 1)$ with the sample mounted in the cryostat as described in the main text. The background-subtracted \mathbf{Q} and energy scans were analyzed using a pseudo-Voigt profile to parameterize the peak line shape in a model-independent manner. The intensity was described as a linear combination of Lorentzian and Gaussian contributions sharing a common full width at half maximum (FWHM) w ,

$$I(E) = A \left[\mu L(E; E_0, w) + (1 - \mu) G(E; E_0, w) \right] + I_{\text{off}}, \quad (2)$$

where A is the peak amplitude, E_0 the peak center, I_{off} a constant residual baseline, and μ the Lorentzian mixing fraction. The Lorentzian and Gaussian components were defined such that they are normalized to unity at $E = E_0$ and reach half maximum at $|E - E_0| = w/2$, so that w corresponds directly to the peak FWHM in energy. Across the investigated temperature range, the fitted mixing coefficient was found to vary within $\mu \simeq 0.12$ – 0.22 , indicating a predominantly Gaussian line shape with a finite Lorentzian component.

In the L scans an additional temperature-independent peak at $L \simeq 0.88$ r.l.u. is attributed to an impurity/spurious contribution and is explicitly accounted for in the fits (via an extra Gaussian term) to avoid biasing the magnetic peak near $L \simeq 1$.

Fewer data points were collected between 10 and 80 K, where no evolution was expected and is confirmed experimentally, and was made denser (typical step ~ 2 K) in the temperature window of interest around the transition (between 80 K and 130 K), above ~ 130 K the magnetic signal becomes comparable to residual noise such that the relative uncertainty on the fitted amplitude exceeds 100%, and these points are therefore shown with their error bars but are not used for reliable extraction of widths/FWHM. To note that the FWHM extracted along HH and L at low temperature around 10 K are the same (around 0.05 (r.l.u.)) to the FWHM of selected nuclear Bragg peaks measured under identical instrumental conditions.

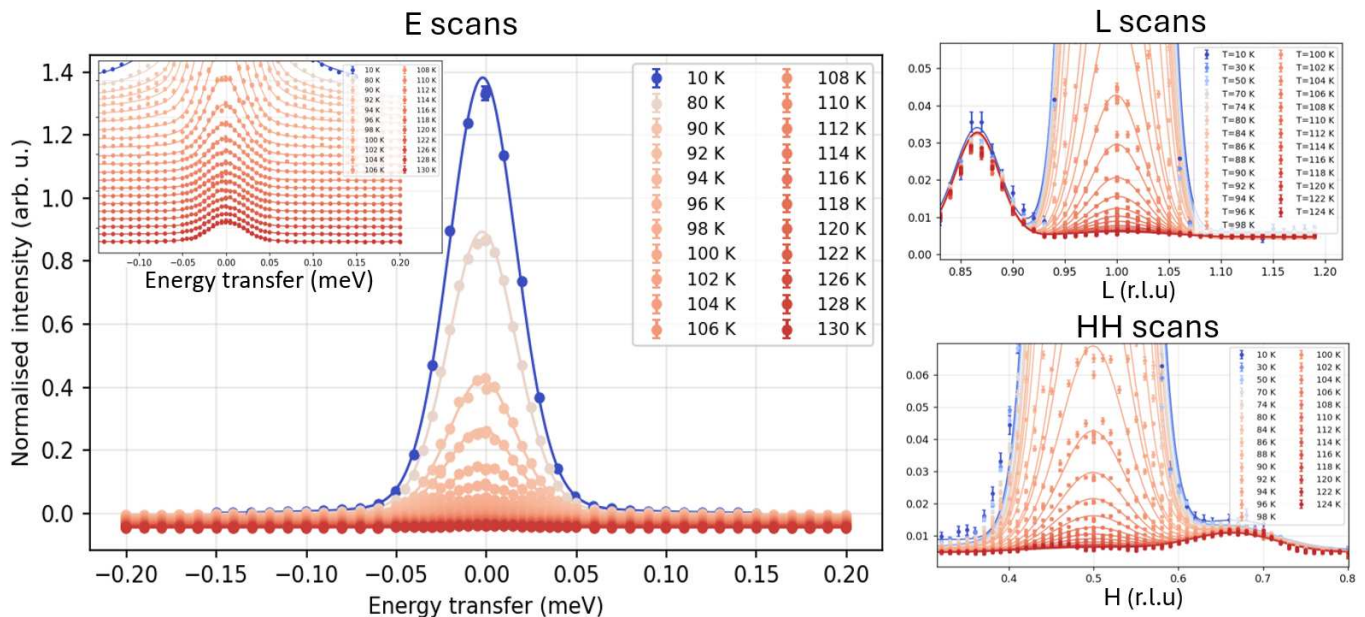


FIG. 6. **Temperature evolution of the magnetic Bragg peak (0.5, 0.5, 1).** Normalized intensity scans are shown as a function of energy transfer E (left), and as momentum scans along L (top right) and along (H, H) (HH, bottom right), for temperatures from **10 K to 130 K** (colour scale from low to high T). Experimental data are shown as symbols with error bars, and the corresponding fits are shown as solid lines. The inset in the E -scan panel shows a **zoom-in on the weak-intensity spectra**; for clarity, each spectrum is vertically shifted by an arbitrary constant offset.

[1] A. Kuzmenko, Kramers–kronig constrained variational analysis of optical spectra, Review of scientific instruments **76** (2005).